Characterization of Lithium-Ion Battery Thermal Abuse Behavior Using Experimental and Computational Analysis

Characterization of Lithium-Ion Battery Thermal Abuse Behavior Using Experimental and Computational Analysis

Carlos F. Lopez,[a,*] Judith A. Jeevarajan,[b,,c] and Partha P. Mukherjee[a,**,z]**

[a]*Department of Mechanical Engineering, Texas A&M University, College Station, Texas 77843, USA*
[b]*National Aeronautics and Space Administration, Lyndon B. Johnson Space Center, Houston, Texas 77058, USA*

While the popularity of lithium-ion batteries (LIBs) has increased significantly in recent years, safety concerns due to the high thermal instability of LIBs limit their use in applications with zero tolerance for a catastrophic failure. Industries such as aerospace and automotive must be very stringent in their selection and design of lithium-ion cells and modules to meet safety requirements. A safety issue of particular interest is a scenario called thermal runaway in which one or more exothermic side-reactions occur, leading to elevated temperature ranges that in turn lead to an uncontrollable and excessive release of heat. This work aims to characterize the effect of these reactions by utilizing a thermal abuse model that predicts single-cell behavior when subjected to an elevated-temperature. The experimental test of the thermal safety behavior includes a constant-power heating element to trigger a thermal runaway event. This study takes an existing thermal abuse model and modifies it to emulate the conditions during a constant-power heating test. The result is found to be in agreement with the experimental data for different cell configurations. The influence of convection condition, cell physical configuration, and electrolyte combustion on the cell thermal behavior is also investigated.
 [DOI: 10.1149/2.0751510jes]

Manuscript submitted March 30, 2015; revised manuscript received July 15, 2015. Published August 11, 2015.

As the energy and power densities of lithium-ion batteries (LIBs) continue to increase, the safety risk associated with of the usage of LIBs increases as well. Off-nominal operating conditions such as mechanical abuse, short circuit, over-charge, and high temperatures can lead to critical failure of lithium-ion cells.[1–3] These abuse conditions can initiate thermal runaway within a cell wherein a chain reaction of exothermic side-reactions can cause a cell to reach temperatures of over 600°C. This scenario is typically catastrophic in nature and is characterized by electrolyte vaporization and sometimes combustion.[4] Various safety features including vents, flame retardant additives, current interrupt (CID) and positive thermal coefficient (PTC) devices can minimize the probability and severity of a thermal event on a cell level.[5–7] The relative thermal stability of lithium-ion batteries also varies with electrode material composition,[8,9] manufacturing method,[10] and separator materials.[11,12] An in depth understanding of the thermal behavior during abuse conditions is required to improve the safety of lithium-ion batteries.[13,14]

The thermal behavior of lithium-ion batteries under normal operation has been studied extensively and can be modeled using a coupled thermal-electrochemical model.[15–17] A different approach that captures the side-reactions that occur at elevated temperatures is required to capture abuse behavior and determine safe practices. Many researchers have studied the mechanisms of thermal runaway in an attempt to determine methods of improving LIB safety. Spotnitz and Franklin[18] summarized a general progression of the exothermic reactions that contribute to thermal runaway. First, the solid-electrolyte interphase (SEI) layer, which protects the anode active material from direct reaction with the electrolyte solvent, will begin to decompose at 90 to 120°C. Using accelerated rate calorimetry (ARC) and differential scanning calorimetry (DSC), it has been shown that the SEI reaction peaks at a temperature of 100°C.[19,20] The generated heat is caused by the decomposition of the meta-stable component of the SEI layer and decreases as this species is consumed. It was shown that the heat release was independent of the amount of intercalated lithium but was very sensitive to the surface area of the anode, as this increased the amount of meta-stable SEI.[21] This reaction is expected to be of the form

$$(CH_2OCO_2Li)_2 \rightarrow Li_2CO_3 + C_2H_4 + CO_2 + \frac{1}{2}O_2 \quad [1]$$

where $(CH_2OCO_2Li)_2$ is the meta-stable component and Li_2CO_3 is the stable component of the SEI layer.

Once the SEI layer decomposes, it no longer protects the graphite and the intercalated lithium in the anode will begin to react with the electrolyte solvents at temperatures greater than 120°C. Richard and Dahn[19] and Biensan et al.[22] analyzed the thermal stability of intercalated graphite and found a heat release peak at 120°C, although the exact peaks vary with the solvents used in the electrolyte. Some possible reactions of intercalated lithium with electrolyte solvent include

$$2Li + C_3H_4O_3\,(EC) \rightarrow Li_2CO_3 + C_2H_4 \quad [2]$$

$$2Li + C_3H_6O_3\,(DMC) \rightarrow Li_2CO_3 + C_2H_6 \quad [3]$$

$$2Li + C_4H_8O_3\,(EMC) \rightarrow Li_2CO_3 + C_3H_8 \quad [4]$$

where the contribution from each reaction will vary with the content of each solvent in the electrolyte.

The first two reactions in the anode can heat the cell to temperatures where the positive active material can decompose and release oxygen and/or react with the electrolyte solvent, beginning at approximately 170°C. The activation energy, reaction enthalpy, and frequency factor for the $LiCoO_2$ positive-solvent reaction have been measured using ARC and X-ray diffraction by MacNeil and Dahn.[23] These researchers also compare the thermal stability of numerous other charged cathode materials, though they only report onset/peak temperature and heat release of thermal runaway.[24] Kong et al.[25] showed that the gases released from the cathode during normal operation was independent of the cathode material, but did vary among $LiCoO_2$, $LiMn_2O_4$, and $LiFePO_4$ when cells were overcharged. The cathode reaction is characterized by decomposition and release of oxygen followed by possible combustion with the electrolyte solvents shown as

$$Mn_2O_4 \rightarrow Mn_2O_3 + \frac{1}{2}O_2 \quad [5]$$

$$3O_2 + C_3H_6O_3\,(DMC) \rightarrow 3CO_2 + 3H_2O \quad [6]$$

for $LiMn_2O_4$ spinel cathode and dimethyl carbonate electrolyte solvent.

*Electrochemical Society Student Member.
**Electrochemical Society Active Member.
[c]Present address: Electrochemical Safety, Underwriter's Laboratories Inc., Northbrook, Illinois 60046, USA.
[z]E-mail: pmukherjee@tamu.edu

Lastly, any electrolyte that remains after the reactions with the negative and positive electrodes can decompose at temperatures greater than 200°C. The heat generated from electrolyte decomposition combined with heat released during combustion with released oxygen can elevate cell temperatures to over 600°C. Previous work has shown that the thermal stability of $LiPF_6$-EC:EMC electrolyte is dependent on component concentrations and heating rate using DSC.[22,26] The exact decomposition reaction, trigger temperature, and released heat are dependent on the solvent in question.[27]

Abuse testing cells by subjecting them to off-nominal conditions can provide valuable insight into the probability and severity of a thermal runaway scenario. Various abuse conditions including overcharge, short-circuit, nail penetration, and oven tests each provide a different avenue to a runaway reaction.[3] As a standard test for cell safety, oven tests in particular are able to characterize the trigger temperature and heat released during a thermal event for a single cell. Since experimental testing is costly, researchers often look to numerical modeling to study thermal abuse behavior of lithium-ion cells. Using experimental oven test data and reaction parameters acquired via calorimetry, Hatchard et al.[28] created a one-dimensional oven test model for both 18650 cylindrical and prismatic cells. The model accurately captured the effect of cell size, electrode material, surface area of the anode, and cell surface emissivity on cell temperature and was verified with experimental data.[29] Spotnitz et al.[18] developed a model that simulated more abuse scenarios including oven test, short-circuit, overcharge, nail penetration, and crush test for multiple cathode materials. This work reports that reactions of the binder are insignificant when compared to the other reactions. Kim et al.[30] then expanded the one-dimensional thermal abuse model to three dimensions to capture the effect of large-cell geometry and spatial variance in temperature. They found that for large cells local hot spots can form that trigger thermal runaway sooner than predicted with 1-D or lumped models. Since small cells are able to reject heat faster than large format cells, the internal temperature gradients of large prismatic cells are critical to the modeling of thermal runaway. Guo et al.[31] also developed a three-dimensional thermal abuse model that included both $LiCoO_2$ and $LiFePO_4$ cells ranging from 18650 cylindrical cell to large format (55 Ah) cells for electric vehicles. Spotnitz[32] expanded the abuse model to three dimensions as well, and showed that cells in contact with each other were more likely to go into thermal runaway. Additionally, Peng et al.[33] outlined the significance of the surface heat transfer condition on thermal runaway onset and severity.

To determine the probability and severity of thermal runaway, a constant-power single-cell heating test is often performed. This test consists of heating a "trigger" cell using a thin-film heating element until thermal runaway is achieved. The temperature response of the cell during this constant heat flux test can be used to determine under what conditions the cell is most susceptible to thermal runaway. The results of this test can also be used to relatively compare different cell designs in the context of thermal safety. The objective of this work is to model the thermal behavior of cells of 18650 cylindrical spiral-wound and prismatic spiral wound cells subjected to elevated temperatures via the constant power heating test. The thermal behavior of these cells can be used to analyze their safety in the context of battery modules.

Methodology

A lithium-ion battery consists of several layers of cathode, anode, separator, current collectors and electrolyte. In cylindrical cells, one unit layer of components is wound in a spiral and inserted into a cylindrical can. Shown in Figure 1, the cell properties used in this work are that of a $LiCoO_2$ cathode, graphite anode, and $LiPF_6$/EC:EMC:DMC electrolyte, as they are well reported in literature. The first cell of interest is a $LiCoO_2$ cylindrical spiral-wound cell of the 18650 design that has a capacity of 2.8 Ah, charge voltage of 4.3 V, discharge cutoff voltage of 3.0 V, a diameter of 18 mm, and height of 65 mm. The second cell is a prismatic spiral-wound cell that has a combination of spinel and nickel oxide cathode active material and a capacity of 5.3 Ah, charge voltage of 4.2 V, discharge cutoff voltage of 2.75 V, a length of 37.3 mm, width of 19 mm, and height of 64.8 mm. Differences in the manufacturing process, thermal mass, and vent location cause their abuse behavior to differ.

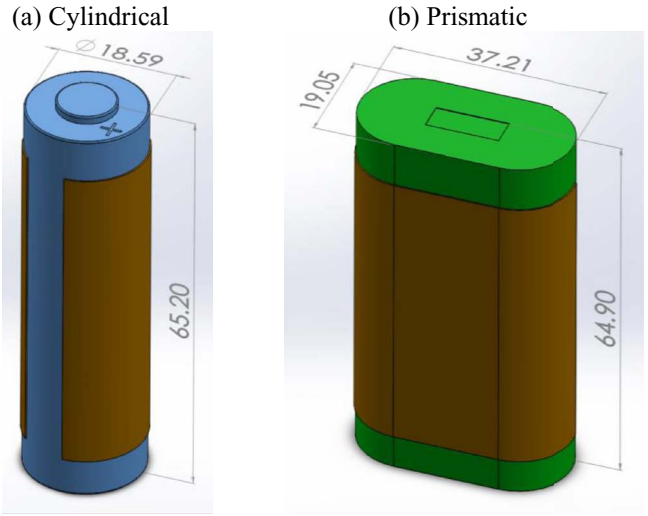

Figure 1. (a) Cylindrical spiral-wound and (b) prismatic spiral-wound test cells. Dimensions shown in millimeters.

Thermal abuse model.— The thermal abuse model used in this work is based on the framework outlined by Hatchard et al.[28] and Kim et al.[30] The model consists of solving for the temperature field inside a cylindrical cell using the principle of thermal energy conservation with zero flux and convection/radiation boundary conditions for the central axis and outer surface respectively (axial symmetry is assumed). Convection heat transfer either cools or heats the cell depending on whether the cell temperature is greater or less than the oven temperature. The various side reactions that occur during thermal runaway are modeled using the Arrhenius equation for each reaction, where the reaction parameters are determined from previous calorimetry experiments. Each reaction contributes to the heating of the cell during thermal runaway via the heat generation term in the thermal energy balance. Additionally, the amount of reacting species for each side reaction is calculated using conservation of mass at each time step. The details of each of these model components are outlined in the following section.

The thermal energy conservation equation governs the behavior of the cells during the thermal abuse test and is given as

$$\rho c_p \frac{\partial T}{\partial t} = \nabla \cdot k \nabla T + Q_{gen} \quad [7]$$

where $\rho\,(\mathrm{kg\,m^{-3}})$ is the cell density, $c_p\,(\mathrm{J\,kg^{-1}K^{-1}})$ is the specific heat capacity of the cell, $T\,(\mathrm{K})$ is the temperature, $t\,(\mathrm{s})$ is time, $k\,(\mathrm{W\,m^{-1}\,K^{-1}})$ is the cell thermal conductivity, and $Q_{gen}\,(\mathrm{W\,m^{-3}})$ is the total heat generation from the various side reactions occurring during the abuse test. The initial temperature for all simulations is assumed to be 28°C. The thermo-physical properties of the various cell components are given in Table I for the 18650 cell. The complete cell properties are evaluated using weighted averaging and are taken to be isotropic with the exception of thermal conductivity, which is anisotropic in nature due to the layering of the cell components. Since the energy conservation equation is solved numerically in the radial direction, the thermal conductivity is calculated by the expression

$$k_n = \frac{\sum_i l_i}{\sum_i l_i / k_i} \quad [8]$$

Table I. Cell specifications and thermo-physical properties.

Component	Material	ρ (kg m^{-3})	c_p (J kg^{-1} K^{-1})	k (W m^{-1} K^{-1})
Positive[31]	$LiCoO_2$	2500	700	1.48
	Aluminum	1500	903	238
	PVDF	1750	1120	0.12
Separator[31]	PP/PE/PP	492	1978	0.334
Negative[31]	Graphite	2660	1437	1.04
	Copper	8900	385	398
	PVDF	1750	1120	0.12
Electrolyte[31]	$LiPF_6$/ EC:DMC:EMC	1290	133.9	0.45

where k_n (W m^{-1} K) is the normal direction thermal conductivity, l_i (m) is a layer's thickness, and k_i (W m^{-1} K) is a layer's thermal conductivity, taken from Table I.

The boundary conditions of the cell are taken to be the no flux condition along the center axis of the cells and the convection condition plus heat flux from the heater on the external surfaces of the cells, given as

$$q''_{conv} = h\,(T_{can} - T_{amb}) - \frac{I\,V}{A_h} \quad [9]$$

where q''_{conv} (W m^{-2}) is the boundary convective heat flux, h (W m^{-2} K^{-1}) is the convection heat transfer coefficient, T_{can} (K) is the can surface temperature, T_{amb} (K) is the ambient temperature, I (A) is the heater current, V (V) is the heater voltage A_h (m^2) is the heater contact area. During conventional oven testing, the convection coefficient is considered to be approximately a constant value as actively controlled blowers maintain the oven temperature and the heater is not used. In the modified oven test, the resistive heater is the primary source of heat and is considered to be a heat flux into the cell. At elevated temperatures, radiation heat transfer from the cell is also considered as a boundary condition, given as

$$q''_{rad} = \varepsilon\sigma\left(T^4_{can} - T^4_{amb}\right) \quad [10]$$

where q''_{rad} (W m^{-2}) is the boundary radiation heat flux, ε is the cell surface emissivity, and σ (W m^{-2} K^{-4}) is the Stefan-Boltzmann constant.

The current implementation of the thermal abuse model considers the SEI decomposition, negative lithium-solvent, positive active material-solvent, electrolyte decomposition, and electrolyte combustion reactions. The abuse model parameters used in this work are shown in Table II for $LiCoO_2$. The combustion reaction component is only taken into account if the conditions of the test and the cell configuration would typically lead to ignition of the gaseous electrolyte. The total heat generation associated with the abuse reactions is formed as a source term in the thermal energy equation and given as

$$Q_{gen} = Q_{sei} + Q_{ne} + Q_{pe} + Q_e \quad [11]$$

where the four right terms are the heat generated during the SEI decomposition, negative lithium-solvent reaction, positive active material-solvent reaction, and electrolyte decomposition, respectively, all in units of (W m^{-3}).

Beginning at approximately 90°C, the solid-electrolyte interphase layer can break down and release heat as it is in a meta-stable state. The rate of reaction for the SEI decomposition is given as

$$R_{sei} = A_{sei}\exp\left[-\frac{E_{a,sei}}{RT}\right]c_{sei}^{m_{sei}} \quad [12]$$

where R_{sei} (s^{-1}) is the SEI reaction rate, A_{sei} (s^{-1}) is the SEI decomposition frequency factor, $E_{a,sei}$ (J mol^{-1}) is the reaction activation energy, R (J mol^{-1} K^{-1}) is the gas constant, T (K) is the local cell temperature, c_{sei} is the dimensionless concentration of meta-stable species containing lithium in the SEI layer, and m_{sei} is the reaction order. The heat generated and the change in reacting species content during this reaction is given as

Table II. Thermal abuse model parameters.

Parameter	Description	Value	Reference
A_{sei}	Frequency factor (s^{-1})	1.667×10^{15}	28,30
A_{ne}		2.5×10^{13}	28,30
A_{pe}		6.667×10^{13}	28,30
A_e		5.14×10^{25}	18,30
$E_{a,sei}$	Activation energy (J mol^{-1})	1.3508×10^5	28,30
$E_{a,ne}$		1.3508×10^5	28,30
$E_{a,pe}$		1.396×10^5	30
$E_{a,e}$		2.74×10^5	18,30
H_{sei}	Reaction heat (J kg^{-1})	2.57×10^5	18,28,30
H_{ne}		1.714×10^6	18,28,30
H_{pe}		3.14×10^5	18,28,30
H_e		1.55×10^5	18,30
c_{sei0}	Initial dimensionless content	0.15	28,30
c_{ne0}		0.75	28,30
α_0		0.04	28,30
c_{e0}		1	28,30
m_{sei}	Reaction order	1	28,30
m_{ne}		1	28,30
m_{pe1}		1	28,30
m_{pe2}		1	28,30
m_e		1	30
t_{sei0}	Initial SEI thickness	0.033	28,30
W_c	Material content (kg m^{-3})	1.39×10^3	30
W_p		1.3×10^3	30
W_e		5.0×10^2	30

$$Q_{sei} = H_{sei}\,W_c\,R_{sei} \quad [13]$$

$$\frac{dc_{sei}}{dt} = -R_{sei} \quad [14]$$

where Q_{sei} (W m^{-3}) is the volumetric heat generation, H_{sei} (J kg^{-1}) is the specific heat release, and W_c (kg m^{-3}) is the carbon content per volume.

Next in the reaction sequence is the reaction between intercalated lithium in the anode and the electrolyte, effectively forming a second SEI layer beginning at approximately 120°C. The rate of the negative-solvent reaction is given as

$$R_{ne} = A_{ne}\exp\left[-\frac{t_{sei}}{t_{sei,ref}}\right]c_{ne}^{m_{ne}}\exp\left[-\frac{E_{a,ne}}{RT}\right] \quad [15]$$

where R_{ne} (s^{-1}) is the reaction rate, A_{ne} (s^{-1}) is the frequency factor, t_{sei} is the SEI thickness, $E_{a,ne}$ (J mol^{-1}) is the reaction activation energy, c_{ne} is the dimensionless concentration of lithium in the anode, and m_{ne} is the reaction order. The heat generated and the change in reacting species content during this reaction is given as

$$Q_{ne} = H_{ne}\,W_c\,R_{ne} \quad [16]$$

$$\frac{dt_{sei}}{dt} = R_{ne} \quad [17]$$

$$\frac{dc_{ne}}{dt} = -R_{ne} \quad [18]$$

where Q_{ne} (W m^{-3}) is the volumetric heat generation, and H_{ne} (J kg^{-1}) is the specific heat release.

The reaction between the cathode active material and the electrolyte begins to occur at 170°C and is very exothermic. The heat released during the negative-solvent reaction can often be enough to initiate this reaction. The rate of the positive-solvent reaction is given as

$$R_{pe} = A_{pe}\alpha^{m_{pe}}(1-\alpha)^{m_{pe}}\exp\left[-\frac{E_{a,pe}}{RT}\right] \quad [19]$$

where R_{pe} (s^{-1}) is the reaction rate, A_{pe} (s^{-1}) is the frequency factor, α is the active material degree of conversion, m_{pe} is the reaction order, and $E_{a,pe}$ ($J\,mol^{-1}$) is the reaction activation energy. The heat generated and the change in reacting species content during this reaction is given as

$$Q_{pe} = H_{pe} W_p R_{pe} \quad [20]$$

$$\frac{d\alpha}{dt} = -R_{pe} \quad [21]$$

where Q_{pe} ($W\,m^{-3}$) is the volumetric heat generation, H_{pe} ($J\,kg^{-1}$) is the specific heat release, and W_{pe} ($kg\,m^{-3}$) is the active material content per volume in the cathode.

The decomposition of the remaining electrolyte typically begins at 200°C. The rate of the positive-solvent reaction is given as

$$R_e = A_e \exp\left[-\frac{E_{a,e}}{RT}\right] c_e^{m_e} \quad [22]$$

where R_e (s^{-1}) is the reaction rate, A_e (s^{-1}) is the frequency factor, $E_{a,e}$ ($J\,mol^{-1}$) is the reaction activation energy, c_e is the dimensionless concentration of the electrolyte, and m_e is the reaction order. The heat generated and the change in electrolyte concentration during this reaction is given as

$$Q_e = H_e W_e R_e \quad [23]$$

$$\frac{dc_e}{dt} = -R_e \quad [24]$$

where Q_e ($W\,m^{-3}$) is the volumetric heat generation, H_e ($J\,kg^{-1}$) is the specific heat release, and W_e ($kg\,m^{-3}$) is the electrolyte content per volume. Electrolyte combustion is considered to be an additional heat released during the decomposition reaction and is accounted for by increasing the heat release for this reaction.

The thermal energy conservation equations are solved in the radial dimension with the appropriate boundary conditions implemented in Battery Design Studio.[34] The present simulations use a mesh size of 50 nodes and an adaptive time-step backward differencing scheme to accurately capture the quick temperature rise during the thermal event in an efficient manner within the STAR-CCM+ simulation framework. The conventional oven test results were validated against experimental results from Hatchard et al.,[28] as shown in Figure 2.

Experimental method.— Conventional oven test procedures consist of pre-heating an oven to the desired temperature and inserting the cell into the chamber at the start time. Some oven tests ramp the oven temperature slowly over time similar to the operation of an accelerated rate calorimeter. Once the desired temperature is achieved it is held constant before, during, and after a thermal event occurs. This ensures the complete reaction of the products in the cell. During the test, the cell can temperature is measured, typically on the surface, in one or more locations depending on the form factor of the cell. This test is well suited for the characterization of the abuse tolerance of a single cell.

The heater test studied in this work is typically conducted in an enclosed chamber and consists of applying heat using a thin, 2 inch square, 40 W heater (manufactured by Omega Engineering Inc., model KHLV-202/10-P) to the surface of a cell and monitoring the temperature response. This type of test is commonly used to test a multi-cell module for abuse tolerance as it is relatively inexpensive to perform since precise temperature control of the test article is not required. This test represents the worst case abuse scenario because it ensures that thermal runaway will occur in the heated cell, and often leads to the propagation of thermal runaway to adjacent cells in a module. Research concerned with the propagation of thermal runaway in a module uses the constant power heater test because the temperature of the adjacent cells can be measured easily with thermocouples and/or infrared cameras. This test protocol also forms the base for module-level abuse test, which will be reported in a follow-on publication. Figure 1 shows the cylindrical and prismatic spiral-wound cells with the flexible heater installed using adhesive. During the test, the "trigger" cell is heated until a thermal runaway event occurs. The surface temperatures of the cells were monitored using K-type thermocouples, typically one per cell for multi-cell tests. The cell temperatures, along with ambient temperature measured at least 8 inches from the test article, were sampled at a rate of 10 Hz for the duration of the tests.

For tests with the cells in a parallel electrical configuration, a single bank voltage is monitored during the test. The individual cell voltages and the series string voltage are monitored during the tests with modules that had serial electrical configurations. The test articles were either 4-cell or 9-cell modules. Additionally, two cameras captured videos of the test from two angles, allowing for the identification of a thermal event. Numerous still images were taken before and after each test to document the test article configuration and post-test damage. All test articles in this work were pre-cycled with at least two full charge-discharge sequences, and tested at 100% state-of charge. Lastly, the open circuit voltages (OCV) of the tested cells were measured before the test to verify that they had been appropriately charged, and after the test to characterize the internal damage of the cell.

The cylindrical 18650 cells have vents located on the top of the cell that allows for an internal pressure release when the electrolyte

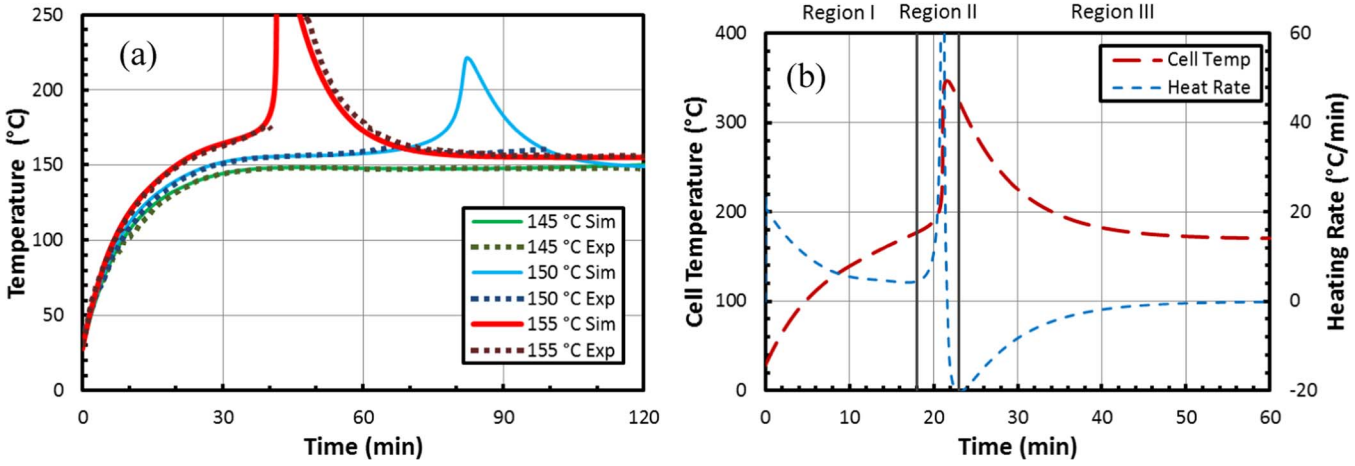

Figure 2. (a) Simulated and experimental cell temperature response for oven tests at 145, 150, and 155°C for a lithium-cobalt-oxide 18650 cell. Results are in agreement with the work of Hatchard et al.[28] (b) Typical calculated cell temperature and heating rate for a simulated 170°C oven test of the same cell. The cell thermal behavior can be divided into three regions: initial heating (I), thermal event rapid heating (II), and final cooling (III).

vaporizes. However, the prismatic cell has two vents located on the flat side of the cell. These side-facing vents can also be problematic in multi-cell modules, as the hot electrolyte vapors and fire are pointed toward neighboring cells, facilitating the propagation of the thermal runaway condition. The cells were placed in a standing configuration to ensure that the cell vents were unobstructed for both form factors. For both cells, most tests induced venting, but only the prismatic cell demonstrated a sustained electrolyte flame, causing additional heat release.

The test procedure can be divided into three regimes. The first consists of heating a cell with a resistive heater supplied with constant power (constant current and voltage). The heater was supplied with 20 V and 1 A for all tests in this study for a power of 20 W. The second regime is where the majority of the reaction heat is released, and is generally referred to as when the "thermal event" occurs. The heater power is disabled once an event occurs. Cells often will vent gaseous electrolyte or rupture in this regime. Lastly, the final regime consists of the cooling of the cell back to environmental temperature. The temperature decay in this regime depends on the heat capacity of the test articles, environmental conditions, and whether the electrolyte combusts. It is important to note that a nitrogen gas pre- and post-test purge was used due to its inert nature that prevented further cell reactions and improved test safety.

Results and Discussion

The thermal behavior of Li-ion cells of cylindrical and prismatic spiral-wound form factor was numerically simulated when subjected to both the standard oven abuse test and a constant-power heater test. The modified oven test is also conducted on the cells and the resulting thermal behavior is compared to the numerical results. The relative contribution of various exothermic side reactions is compared for the conventional and modified oven tests under various conditions and configurations. Additionally, the effect of convective heat transfer condition on the cell behavior when subjected to both tests is reported. In the following sections, "simulated" and "calculated" refer to model predictions whereas "experimental" and "measured" refer to experimental test data.

Effect of oven temperature.— The simulated and experimental temperature responses of an 18650 cell at oven temperatures of 145, 150, and 155°C are shown in Figure 2a, adapted from the work of Hatchard et al.[28] The surface heat transfer coefficient is taken to be 7.17 W/m^{2}K and the initial cell temperature is 28°C. The simulated temperature during the 155°C oven test shows a steady rise for the first 40 minutes, and then rapidly spikes in temperature to a maximum of 300°C. This elevated temperature indicates that thermal runaway has occurred in this case. After the runaway event, the cell temperature decreases steadily to match the oven temperature where it remains for the remainder of the test. Next, the 150°C oven test also shows a steady rise in temperature for the first 30 minutes. In contrast, the temperature plateaus for about 40 minutes at 160°C. At the 60 minute mark, the cell begins to heat further, peaking at 82 minutes with a temperature of 221°C. The cell then cools back down to the 150°C oven temperature. Lastly, for the 145°C oven test, the cell heats steadily to a maximum temperature of 150°C during the first 30 minutes, and the slowly decreases to the oven temperature of 145°C. It can also be seen that the experimental results for the same oven temperatures are mostly in agreement with the simulated results with a few exceptions. The most notable deviations are in the timing of the thermal runaway events and maximum temperatures of the cells during the 150 and 155°C oven tests. The validated model does not account for Joule-Thompson cooling from electrolyte venting or for the heat released during electrolyte decomposition, which causes the respective differences in simulated results and experimental data.[28] Later in this work, the electrolyte decomposition reaction is accounted for to better predict the maximum temperature during thermal runaway.

The temperature responses for the 145, 150, and 155°C oven tests show that as the oven temperature increases, the onset of thermal runway occurs faster, and the severity of the runaway event increases as indicated by the higher peak temperature. It can be inferred from these results that onset of thermal runaway is characterized by a critical onset temperature. If a cell should reach and sustain that temperature, thermal runaway will certainly occur. It is shown that this temperature is between 145 and 150°C for the cylindrical 18650 cell tested by Hatchard et al.[28] Focusing on the most extreme case of a 155°C oven, the steady initial rise in temperature shifts to a more accelerated rise around 25 minutes into the test. This is likely when the meta-stable component of the SEI layer in the anode decomposes and the lithium intercalated in the anode graphite reacts with the electrolyte solvent to form a new SEI layer. This reaction pushes the temperature well over the 155°C oven temperature, triggering the positive-solvent and electrolyte decomposition reactions. The 150°C oven test also induces temperatures beyond ambient, though in a more gradual manner so that the peak reaction is delayed by several minutes.

Using the validated model, the same cells were simulated with an oven temperature of 170°C and h = 7.17 W/m^{2}K as depicted in Figure 2b. By calculating the heating rate of the cell from the slope of the temperature response, three thermal behavior regions can be seen. The first region (region I) is characterized by the initial heating of the cell by convection from the air in the elevated temperature oven. The heating rate starts at a maximum value of 20°C/min as the temperature difference between the cell and the environment is the greatest at this point. This heating rate decreases steadily as the cell heats as the temperature difference decreases and the heating via convection and radiation decreases. The heating rate then begins to stabilize and plateaus, still decreasing, as the internal heat generated from the SEI decomposition reaction begins. This reaction pushes the cell temperature just above the oven temperature, and initiates the negative-solvent reaction. The minimum heating rate value of 2°C/min at 18 minutes into the test signals the end of region I. Region II begins with the aforementioned negative-solvent reaction which generates enough heat to reverse the trend of the cell heating rate from decreasing to increasing. At this time, the cell temperature is elevated enough to trigger the positive-solvent reaction, which in combination with the negative-solvent reaction, heats the cell to above 340°C over a very short period of time. Once the reacting species is consumed, the cell no longer generates heat, and heat rejection from the cell to the surrounding oven cools the cell gradually down to 170°C. Region II ends at the minimum value of heating rate, which represents the maximum cooling condition. This occurs at 23 minutes into this test. Region III is characterized by the cooling of the cell back to ambient conditions. The slope of the temperature response and the magnitude of the heating rate is governed by the heat capacity of the cell, oven temperature, and assumed convection coefficient. The three regions of thermal behavior are referred to during the subsequent analysis. The results indicate that the severity and onset of thermal runaway are positive functions of temperature. A critical or "trigger" temperature can be defined as the temperature at which thermal runaway is imminent.

Effect of convection condition.— It is clear from the results thus far that the ambient cooling condition in the oven chamber, which is controlled by a circulation fan, affects the rate at which the cell temperature increases and decreases. Figure 3 shows the effect of four convection coefficients on the simulated temperature response during conventional oven tests performed on a $LiCoO_2$ 18650 cell at four oven temperatures. As shown previously, higher oven test temperatures result in an increase in probability and severity of a thermal event. While it was shown that there was a critical oven temperature at which a cell would not go into thermal runaway, the results show that increasing the convective heat transfer coefficient also decreases the chance and severity of thermal runaway. For example, Figure 3a shows the simulated temperature during oven tests at 145, 150, 155, and 160°C at h = 5 W/m^{2}K. The peak cell temperature decreases with decreasing oven temperature, until the 145°C test, where there is no noticeable peak in temperature, and therefore no thermal runaway event. This trend continues for the same simulated oven tests

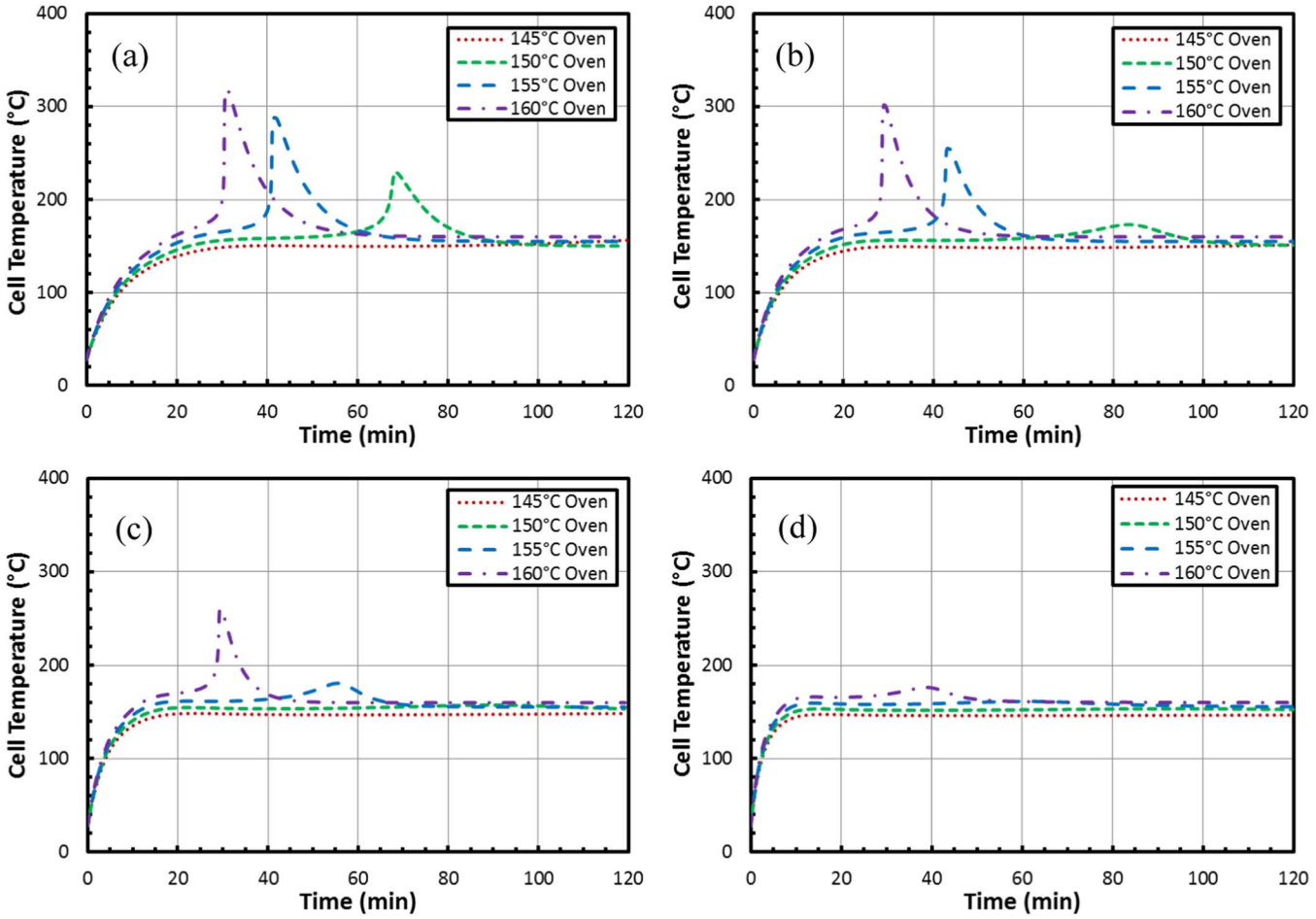

Figure 3. Calculated temperature response for simulated oven tests at 145, 150, 155, and 160°C and environment convection coefficients of (a) 5, (b) 10, (c) 20, and (d) 40 W/m^{2}K.

conducted with an h = 10 W/m^{2}K, shown in Figure 3b. The 155 and 160°C tests both went into thermal runaway, but the 150°C test only showed a minor peak in temperature that took nearly twice the time to reach than the warmer tests. This test also showed the lack of thermal runaway for 145°C oven temperature. As shown in Figure 3c, increasing the convection coefficient to 20 W/m^{2}K decreases the simulated temperature response for all cases and prevents thermal runaway for the 155°C case, which had peak temperature of only 180°C. Lastly, Figure 3d shows the test results for h = 40 W/m^{2}K where none of the oven temperatures showed a temperature rise expected from a thermal runaway event. These results indicate that the critical temperature that triggers thermal runaway is affected by the convective heat transfer experienced by the cell. It is likely that this result translates to radiation heat transfer as well, where the surface emissivity affects the runaway onset temperature. The results that increasing convective heat transfer, leading to a faster rise in cell temperature and higher internal gradient, actually decreases the chances and severity of thermal runaway appear to be counterintuitive at first. However, the reason for this trend is that after the cell reaches the oven temperature, the heat generated from side-reactions is more easily dissipated to the oven environment. For most cases, this causes the heat generated during the SEI decomposition and negative-solvent reactions to be rejected to the oven before the next reactions in the chain can be triggered. This result indicates that cells in better contact with a cooling medium are less prone to thermal runaway even under abuse conditions. The importance of battery thermal management is not to be overlooked when considering abuse scenarios as a thermal runaway event caused by inadvertent abuse may be prevented with sufficient cooling.

Influence of abuse reactions.— To further elucidate the mechanisms of thermal runaway, the calculated temperature evolution, heat rates, and concentrations of the reacting species are shown in Figure 4 for simulated oven tests at 150°C (test 1) and 170°C (test 2) with h = 7.17 W/m^{2}K. These oven temperatures were chosen because one is characterized by severe thermal runaway and the other by the lack of a thermal event. The oven test was simulated by exposing the cells to a constant oven temperature. Figure 4a shows the calculated cell temperature and heating rate for the two oven tests. During the initial heating in region I, the 170°C test cell temperature rises faster, reaching 170°C in about 16 minutes. The 150°C test cell does not reach the oven temperature until 21 minutes into the test. This difference is further highlighted by the substantially higher heating rate for the 170°C test, and can be explained by the dependence of convection heat transfer on the difference between the surface and ambient temperatures. This difference in initial heating rate affects the onset of the SEI decomposition, depicted by Figure 4b, which shows the amount of lithium containing meta-stable species in the SEI layer. Since the 170°C test heats the cell faster, the SEI decomposes first for this test and over a shorter duration than the 150°C case. Additionally, Figure 5 shows that the calculated heat generated by the SEI decomposition reaction is 40% greater for the 170°C test and is released in nearly half the time of the 150°C reaction.

Several differences between the two tests are noted in region II, the event zone. First, the 170°C test cell temperature begins to rise faster after reaching its oven temperature as indicated by the change in the heating rate trend from decreasing to increasing. The 150°C test cell temperature rises beyond the oven temperature, but only by 5°C. This subtle rise in simulated temperature is caused by the

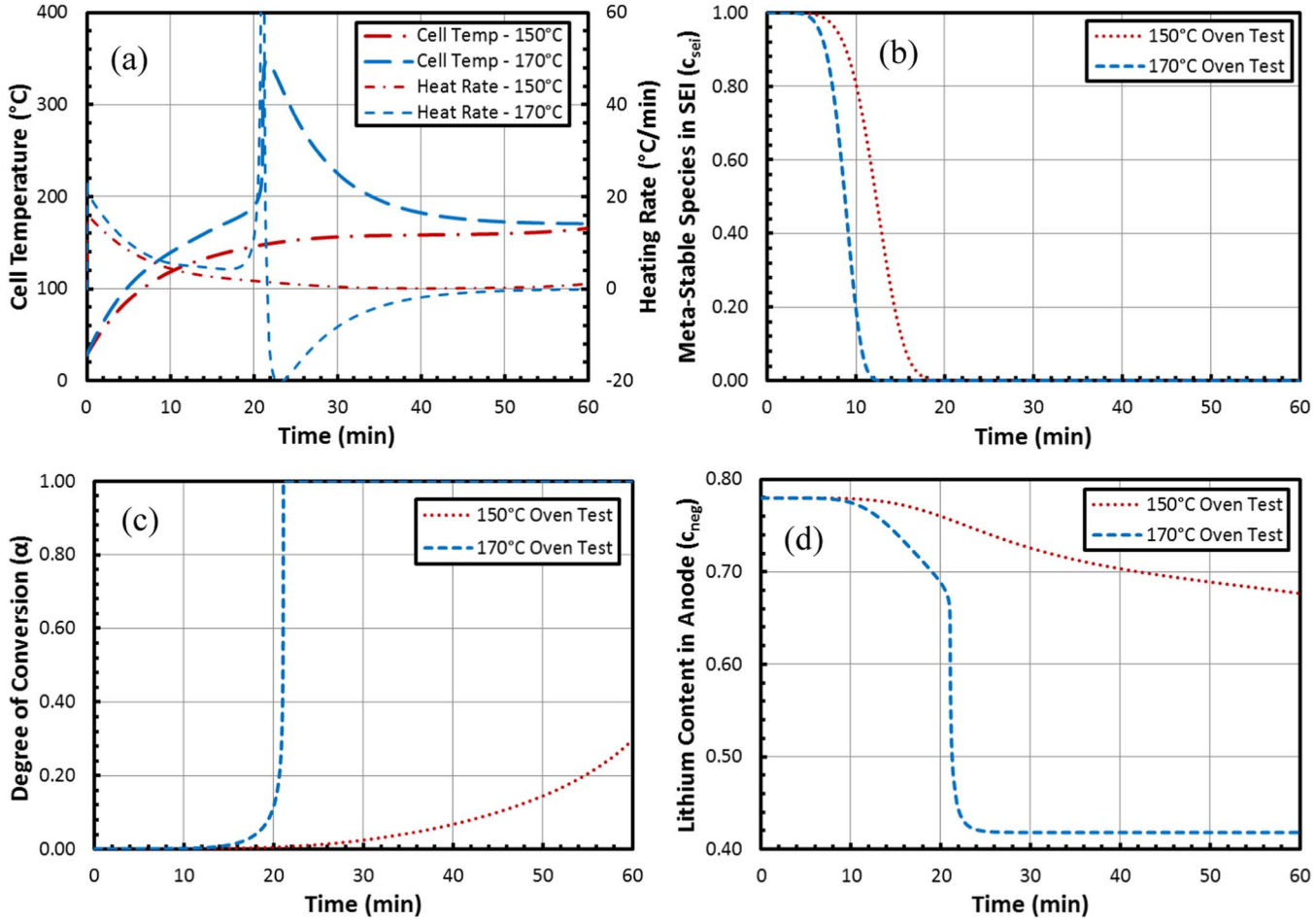

Figure 4. Calculated (a) temperature and heating rate, (b) amount of meta-stable SEI, (c) cathode degree of conversion, and (d) anode lithium content during simulated oven tests at 150 and 170°C with a convection coefficient of 7.17 W/m^{2}K.

negative-solvent reaction, depicted in Figure 4d, which shows the decrease in lithium intercalated in the anode as it reacts with the solvent. From 10 to 20 minutes, the anode lithium content for the 170°C test steadily decreases until the thermal event when it plummets to its minimum value of 0.41. The negative lithium concentration for the 150°C test only steadily decreases throughout the test and approaches a higher final value of 0.68. Since the cell temperature during the 150°C test is much lower than that of the 170°C test, the negative-solvent reaction occurs at a much lower rate delaying thermal runaway. This is further supported by the heat generation

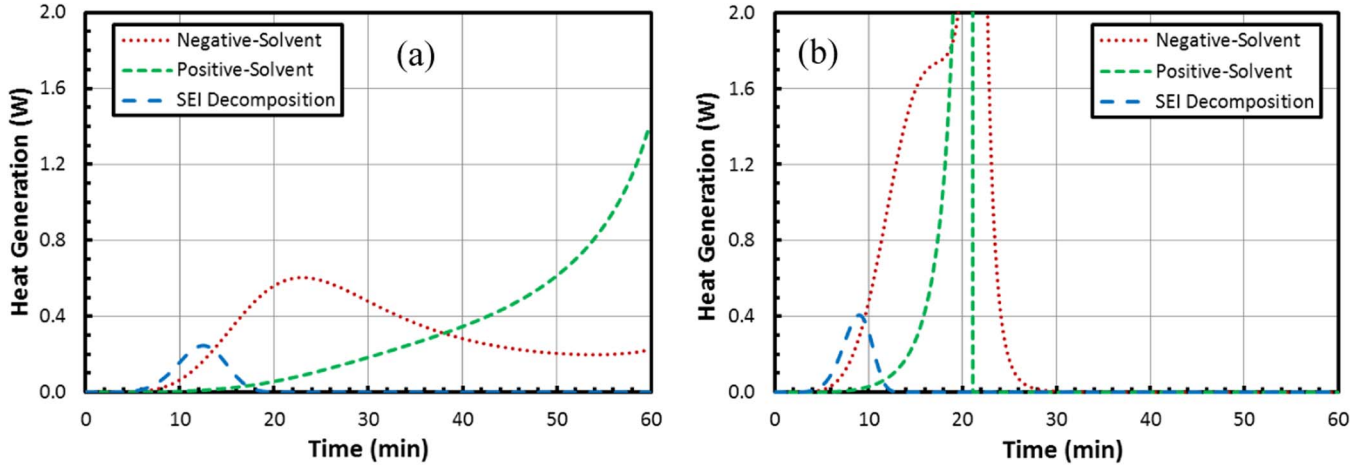

Figure 5. Calculated heat generation for the SEI decomposition, negative-solvent reaction, and positive active material-solvent reaction during simulated (a) 150°C and (b) 170°C oven tests.

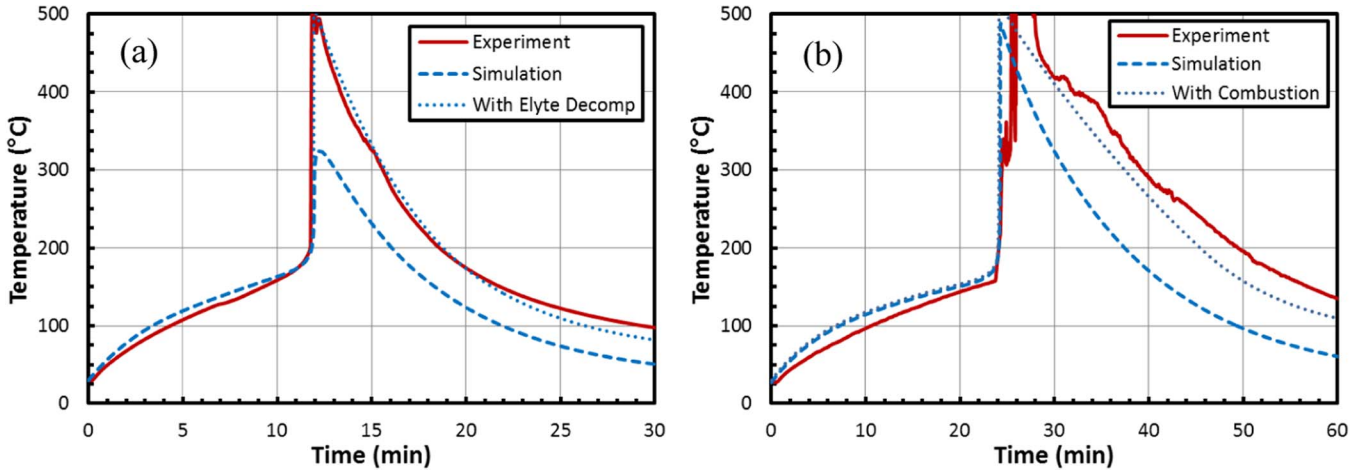

Figure 6. Simulated and experimental temperature response during constant power abuse test for (a) cylindrical and (b) prismatic spiral-wound cells. Note the contribution of the electrolyte decomposition and combustion reactions in these cases.

from the negative-solvent reaction, which rises and then tapers off to a relatively low value for the 150°C oven test, but rises quickly and stays elevated for the 170°C test.

Additionally, the 170°C oven test conditions triggered the cell into thermal runaway while the 150°C test cell was not triggered. This difference is influenced by combined effects of the positive and negative-solvent reactions, where the relevant species concentrations are shown in Figures 4c and 4d. The steady decrease in anode lithium content for the 150°C test indicates that the negative reaction is sluggish, and the large drop in concentration for the 170°C test indicates a quick reaction and a massive heat release leading to a thermal event. The heat released by the negative-solvent reaction directly affects the onset of the positive-solvent reaction. For example, the 150°C oven test degree of conversion very slowly rises throughout the test, whereas the same for the 170°C test rises very rapidly during the thermal event, and reaches unity at the time corresponding to the peak cell temperature.

Lastly, during the cool-down phase, a slight increase in temperature of the 150°C test indicates that the cell reaction is incomplete. In fact, the lithium content in the anode and cathode continues to decrease, and the heat generated by the positive-solvent reaction increases as the test continues. It is possible that should this cell be subjected to the elevated oven temperatures for a sufficiently long duration, it would go into thermal runaway. This indicates that the duration of exposure to thermal abuse conditions could also affect the onset of thermal runaway. Additionally, the results show that the heat generated from the SEI decomposition and negative-solvent reaction directly influences the onset of the positive-solvent reaction. Thermal runaway will certainly occur in the cell if the excess heat generated by these reactions is not dissipated quickly.

Modified oven test.— The thermal responses of cells subjected to the constant power modified oven test are similar in nature to the responses under conventional oven test conditions. The behavior falls into the same three regions described previously: (I) pre-heating, (II) thermal event, and (III) cool down. Figure 6 shows the simulated and experimental thermal behavior of a cylindrical and prismatic spiral-wound cell subjected to the constant-power abuse test. The experimentally measured cylindrical cell response, shown in Figure 6a, is characterized by an initial heating stage, followed by a thermal event that has a peak temperature of over 500°C. However, the simulated response of the same cell under the same conditions only estimates the peak event temperature to be 320°C, a significant under-prediction. Furthermore, the simulated temperature in region III is consistently underestimated by the thermal abuse model. The reason for this difference is likely due to the model not accounting for the electrolyte decomposition reaction up to this point. By including this reaction in the thermal abuse model, a more accurate temperature curve is acquired that closely matches the experimental data.

A similar issue presents itself for the prismatic spiral-wound cell. The prismatic cell temperature during the test, shown in Figure 6b, is reasonably modeled until region III. The peak temperature of over 500°C is captured well by the adjusted model that includes the electrolyte decomposition, but the temperature during the cool-down phase is again underestimated. The likely reason for this discrepancy is that during the experimental test for this cell, the unreacted electrolyte vented from the cell and ignited. The additional heat released during this combustion is not typically accounted for in thermal abuse models and must be included to represent this test condition. This combustion heat is simply added as an additional source term in Equation 11. However, this generated heat may also affect the chamber temperature, so further analysis may be required to capture the residual heat entirely. In summary, to realistically capture the thermal behavior of these cells under a constant flux heating condition, modeling of the electrolyte decomposition and combustion is required.

Influence of physical configuration.— The two form factors tested in this work demonstrated significantly different thermal behaviors. While the cylindrical cell heated, vented, and cooled in a predictable and consistent manner, the prismatic cell tended to be more active with rapid venting and electrolyte ignition. Aside from this difference, the prismatic cell also went into thermal runaway at 24 minutes into test compared to the cylindrical cell's trigger time of 12 minutes. This difference is due to the prismatic cell being nearly twice as massive as the cylindrical cell; 93.5 versus 50 grams. Therefore, the thermal mass of the prismatic cell is significantly greater than that of the cylindrical cell, yielding the slower rise in temperature. Because of this difference, the time scales are normalized when comparing the simulated results of these cells.

Figure 7 shows the simulated temperature evolution and heating rate for both form factors when subjected to the heater test protocol. In the heating region, it is shown that the heating rate for the cylindrical cell is more than double the heating rate for the prismatic cell, due to the aforementioned thermal mass difference. The two cell temperatures in this region align almost exactly with each other on the normalized time scale until close to the onset of thermal runaway. The temperatures deviate when the SEI decomposition and negative-solvent reactions begin to occur. This is indicated by the calculated reactant profiles shown in Figure 8 that are nearly the same for both cases with some slight deviations in the SEI and anode lithium concentrations at the same time as the temperature deviation. The SEI decomposition reaction initiates for the prismatic cell first on the normalized time scale with that for the cylindrical cell occurring after. The same trend holds for the anode lithium content with the

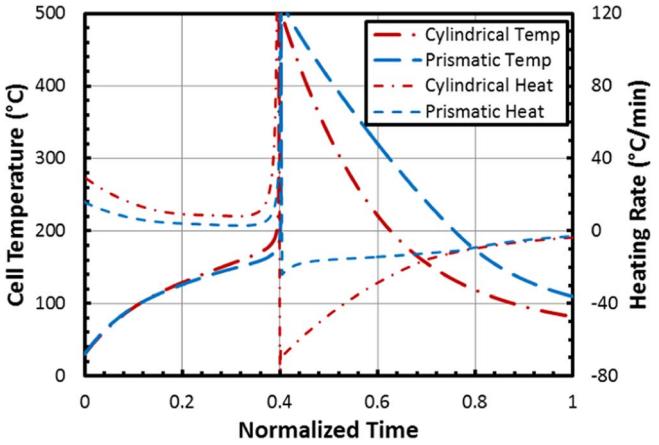

Figure 7. Calculated temperature response and heating rate during a simulated oven test for the cylindrical and prismatic spiral-wound cells.

prismatic reacting first. Additionally, Figure 9 shows that the calculated SEI decomposition and negative-solvent reactions are lower in magnitude for the prismatic cell than that of the cylindrical cell. The slow reactions are also a product of the higher thermal mass associated with the prismatic cell. Since reactions are functions of temperature, reaction rates decreased with a slow temperature rise. Next, the onset temperature of the prismatic cell is about 160°C, which is lower than that of the cylindrical cell, which is about 190°C. This is difference is likely due to the differences in the material composition of the two cells, which also affects the positive-solvent and electrolyte decomposition reactions. Lastly, the difference in temperature response for the cool-down region is entirely due to the combustion of the electrolyte. These results indicate that an increased cell mass decreases the rate at which the temperature responds under thermal abuse conditions.

Effect of convection for modified test.— While the convection coefficient has been shown to have a significant effect on the thermal response during the conventional oven test, convection with the chamber could have a different effect for the modified oven test. Figure 10 shows the simulated temperature for the cylindrical cell at various convection conditions for the heater test. For the initial heating region, it is shown that increasing the convective heat transfer coefficient decreases the temperature rise, which is contrary to the result for the conventional oven test shown in Figure 3. Additionally, the onset of thermal runaway and the peak temperatures of the cells are fairly consistent for the modified tests at the four convection conditions studied, which is different than the result from the conventional tests where increasing cooling condition decreased the chance and severity of thermal runaway. These results are because during the conventional test, convection is used to heat the cell from its initial temperature to the oven temperature, whereas in the modified test, convection works to dissipate the heat transferred to the cell via the flexible heater. Lastly, the decline in cell temperature during the cool-down phase is heavily dependent on the convection condition as low values of h induce a gradual decline and high values of h cause a rapid decline in temperature. Thermal gradients inside the cell could also play a role in abuse behavior. Thermal gradients are typically important when cells are of a large form factor since heat generated in the cell has to travel a greater

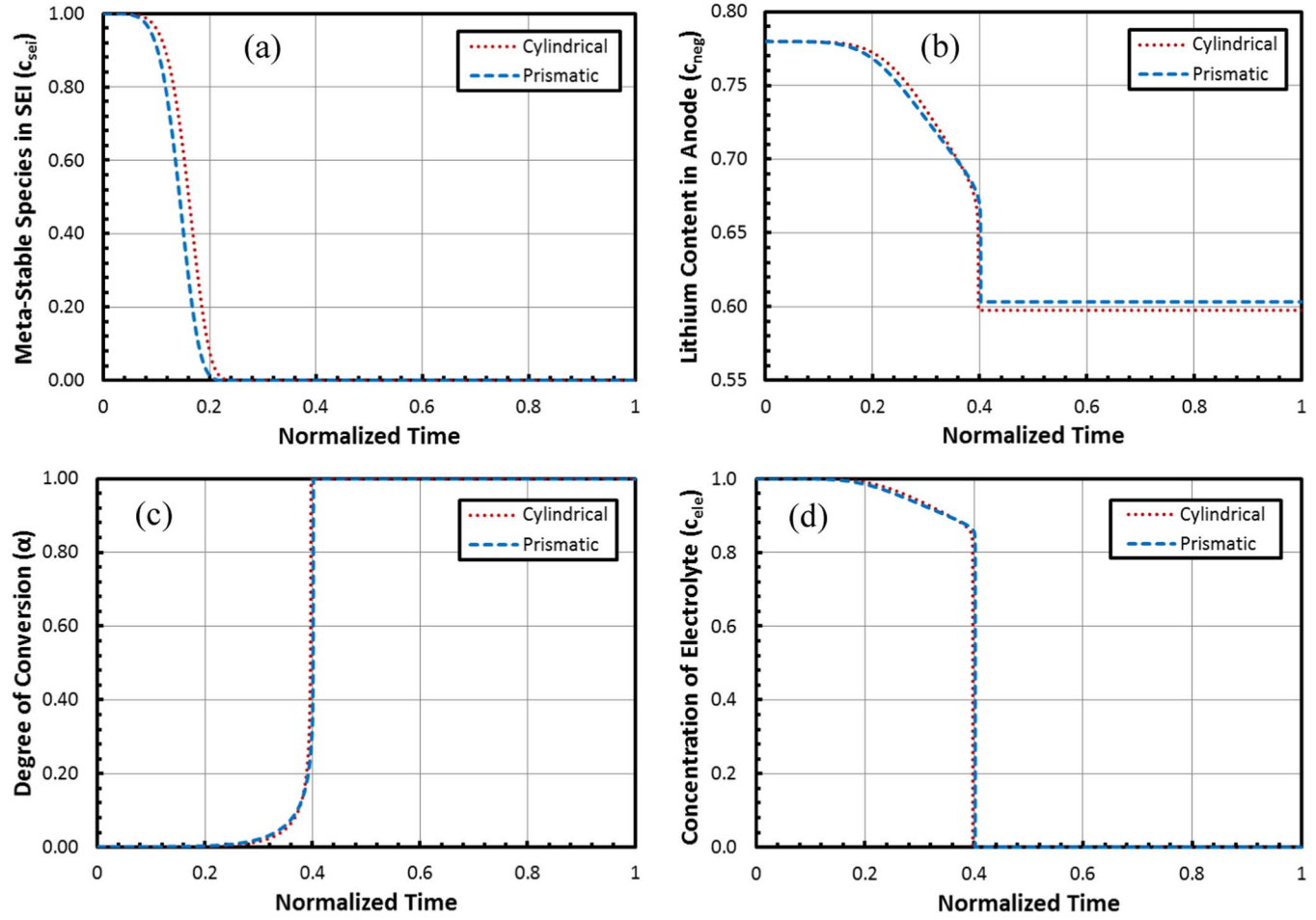

Figure 8. Calculated (a) amount of meta-stable SEI, (b), cathode degree of conversion (c) anode lithium content, and (d) electrolyte concentration during a simulated oven test for the cylindrical and prismatic spiral-wound cells.

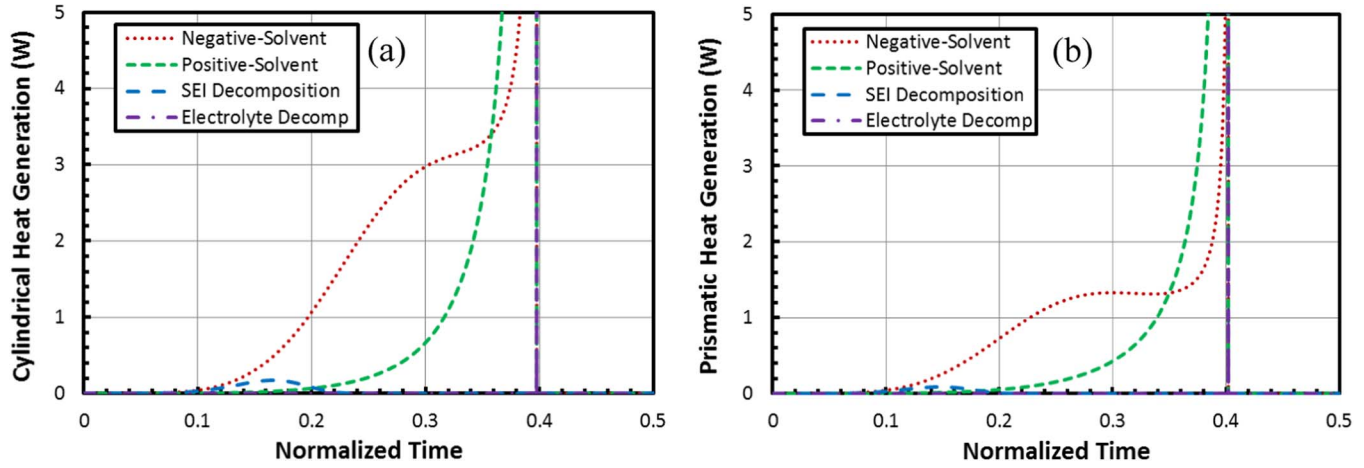

Figure 9. Calculated heat generation for the SEI decomposition, negative-solvent reaction, and positive active material-solvent reaction, and electrolyte decomposition during simulated oven test for (a) cylindrical and (b) prismatic spiral-wound cells.

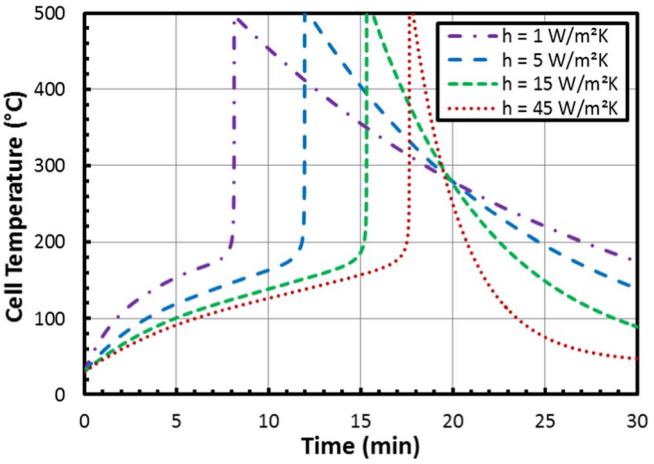

Figure 10. Calculated cell surface temperature for the cylindrical cell at 1, 5, 15, and 45 W/m^{2}K convective heat transfer coefficient for a simulated constant power heating test.

distance before being dissipated. If the cooling condition is high at the surface and/or the cell is very thick, the cell core temperature could be many degrees hotter than the surface temperature, causing thermal runaway to occur sooner than anticipated. In summary, increasing the convection condition delays the onset of thermal runaway significantly, indicating that an adequate battery thermal management system could prevent the onset and propagation of thermal runaway.

Conclusions

In the present work a thermal abuse model is formulated to analyze the thermal runaway behavior of cells subjected to a constant heater power abuse test. This model was derived from conventional oven test protocol where a cell is subjected to a high temperature oven. The modified model was validated against experimental results for conventional oven tests and the effect of oven temperature and convection condition was determined. The probability and severity of thermal runaway increased with increased oven temperature and decreased convection coefficient for conventional oven tests. The abuse reaction sequence was identified as first SEI decomposition, then negative-solvent, and lastly positive-solvent for both the convention and modified oven tests. It was found that the electrolyte decomposition reaction must be included to accurately model 18650 cells subjected to the modified test but was not necessarily required for the conventional test. Additionally, it was found that an electrolyte combustion reaction must be accounted for, should the electrolyte ignite during the heater test. The simulated thermal behavior under constant-power heating condition was found to be in agreement with experiment. Next, the effect of the cell physical form factor was found for the modified test. The additional thermal mass of the prismatic cell caused slower temperature response and sluggish kinetics for the abuse reactions. Lastly, it was found that changing the convection condition had the opposite effect for the heater test than what was found for the conventional test. This was because the heater test represents a constant flux boundary condition whereas the conventional oven test represents a constant temperature boundary condition.

Acknowledgments

The authors acknowledge the NASA Office of Education for financial support on this work. Additionally, the support of the Energy System Test Area at NASA Johnson Space Center was invaluable in this work. CD-adapco and TAMU's computing infrastructure are gratefully acknowledged for their support and for access to the STAR-CCM+ software.

List of Symbols

A_{sei}	SEI-decomposition frequency factor (s^{-1})
A_{ne}	Negative-solvent frequency factor (s^{-1})
A_{pe}	Positive-solvent frequency factor (s^{-1})
A_e	Electrolyte decomposition frequency factor (s^{-1})
$E_{a,sei}$	SEI-decomposition activation energy (J mol^{-1})
$E_{a,ne}$	Negative-solvent activation energy (J mol^{-1})
$E_{a,pe}$	Positive-solvent activation energy (J mol^{-1})
$E_{a,e}$	Electrolyte decomposition activation energy (J mol^{-1})
H_{sei}	SEI-decomposition heat (J kg^{-1})
H_{ne}	Negative-solvent heat (J kg^{-1})
H_{pe}	Positive-solvent heat (J kg^{-1})
H_e	Electrolyte decomposition heat (J kg^{-1})
R_{sei}	SEI-decomposition rate (J kg^{-1})
R_{ne}	Negative-solvent rate (J kg^{-1})
R_{pe}	Positive-solvent rate (J kg^{-1})
R_e	Electrolyte decomposition rate (J kg^{-1})
c_{sei}	Amount of lithium-containing meta-stable species in the SEI
c_{ne}	Amount of lithium in the carbon
α	Degree of conversion
c_e	Concentration of electrolyte
m_{sei}	Reaction order for c_{sei}
m_{pe1}	Reaction order for α
m_{pe2}	Reaction order for (1- α)
m_e	Reaction order for c_e
W_c	Carbon content (kg m^{-3})
W_p	Active material content in cathode (kg m^{-3})

W_e	Electrolyte content (kg m^{-3})
c_p	Heat capacity (J kg^{-1} K^{-1})
h	Heat transfer coefficient (W m^{-2} K^{-1})
k	Thermal conductivity (W m^{-1} K^{-1})
Q	Total heat generation rate (W m^{-3})
Q_{sei}	SEI-decomposition heat generation rate (W m^{-3})
Q_{ne}	Negative-solvent heat generation rate (W m^{-3})
Q_{pe}	Positive-solvent heat generation rate (W m^{-3})
Q_e	Electrolyte decomposition heat generation rate (W m^{-3})
q_{conv}	Heat dissipation rate (W m^{-2})
R	Universal gas constant (J mol^{-1} K^{-1})
T	Temperature (K)
t	Time (s)
T_{surf}	Cell surface temperature (K)
T_{amb}	Oven temperature (K)
ρ	Density (kg m^{-3})

References

1. T. M. Bandhauer, S. Garimella, and T. F. Fuller, *J Electrochem Soc*, **158**, R1 (2011).
2. W. T. J. A. Jeevarajan, Performance and Safety Tests of Lithium-Ion Cells Arranged in a Matrix Design Configuration, in *Space Power Workshop*, Manhattan Beach, CA (2010).
3. J. A. Jeevarajan, Safety Limitations Associated with Commercial 18650 Lithium-ion Cells, in, NASA, Johnson Space Center (2010).
4. Q. S. Wang, P. Ping, X. J. Zhao, G. Q. Chu, J. H. Sun, and C. H. Chen, *J Power Sources*, **208**, 210 (2012).
5. P. G. Balakrishnan, R. Ramesh, and T. P. Kumar, *J Power Sources*, **155**, 401 (2006).
6. D. H. Doughty, E. P. Roth, C. C. Crafts, G. Nagasubramanian, G. Henriksen, and K. Amine, *J Power Sources*, **146**, 116 (2005).
7. M. Kise, S. Yoshioka, and H. Kuriki, *J Power Sources*, **174**, 861 (2007).
8. K. Zaghib, J. Dube, A. Dallaire, K. Galoustov, A. Guerfi, M. Ramanathan, A. Benmayza, J. Prakash, A. Mauger, and C. M. Julien, *J Power Sources*, **219**, 36 (2012).
9. E. P. Roth and D. H. Doughty, *J Power Sources*, **128**, 308 (2004).
10. J. A. Jeevarajan, Hazards, Safety and Design Considerations for Commercial Lithium-ion Cells and Batteries, in *2nd International Association for the Advancement of Space Safety*, NASA, Johnson Space Center, Chicago, IL (2007).
11. M. S. Wu, P. C. J. Chiang, J. C. Lin, and Y. S. Jan, *Electrochim Acta*, **49**, 1803 (2004).
12. S. Tobishima, K. Takei, Y. Sakurai, and J. Yamaki, *J Power Sources*, **90**, 188 (2000).
13. D. H. Doughty, P. C. Butler, R. G. Jungst, and E. P. Roth, *J Power Sources*, **110**, 357 (2002).
14. K. Smith, G. H. Kim, E. Darcy, and A. Pesaran, *Int J Energ Res*, **34**, 204 (2010).
15. W. B. Gu and C. Y. Wang, *J Electrochem Soc*, **147**, 2910 (2000).
16. G. H. Kim, K. Smith, K. J. Lee, S. Santhanagopalan, and A. Pesaran, *J Electrochem Soc*, **158**, A955 (2011).
17. P. P. Mukherjee, S. Pannala, and J. A. Turner, *Handbook of Battery Materials*, 2nd Edition, 843 (2011).
18. R. Spotnitz and J. Franklin, *J Power Sources*, **113**, 81 (2003).
19. M. N. Richard and J. R. Dahn, *J Electrochem Soc*, **146**, 2068 (1999).
20. H. Maleki, G. P. Deng, A. Anani, and J. Howard, *J Electrochem Soc*, **146**, 3224 (1999).
21. D. D. MacNeil, D. Larcher, and J. R. Dahn, *J Electrochem Soc*, **146**, 3596 (1999).
22. P. Biensan, B. Simon, J. P. Peres, A. de Guibert, M. Broussely, J. M. Bodet, and F. Perton, *J Power Sources*, **81**, 906 (1999).
23. D. D. MacNeil and J. R. Dahn, *J Electrochem Soc*, **148**, A1205 (2001).
24. D. D. MacNeil, Z. H. Lu, Z. H. Chen, and J. R. Dahn, *J Power Sources*, **108**, 8 (2002).
25. W. H. Kong, H. Li, X. J. Huang, and L. Q. Chen, *J Power Sources*, **142**, 285 (2005).
26. G. G. Botte, R. E. White, and Z. M. Zhang, *J Power Sources*, **97–8**, 570 (2001).
27. T. Kawamura, A. Kimura, M. Egashira, S. Okada, and J. I. Yamaki, *J Power Sources*, **104**, 260 (2002).
28. T. D. Hatchard, D. D. MacNeil, A. Basu, and J. R. Dahn, *J Electrochem Soc*, **148**, A755 (2001).
29. T. D. Hatchard, D. D. MacNeil, D. A. Stevens, L. Christensen, and J. R. Dahn, *Electrochem Solid St*, **3**, 305 (2000).
30. G. H. Kim, A. Pesaran, and R. Spotnitz, *J Power Sources*, **170**, 476 (2007).
31. G. F. Guo, B. Long, B. Cheng, S. Q. Zhou, P. Xu, and B. G. Cao, *J Power Sources*, **195**, 2393 (2010).
32. R. M. Spotnitz, J. Weaver, G. Yeduvaka, D. H. Doughty, and E. P. Roth, *J Power Sources*, **163**, 1080 (2007).
33. P. Peng, Y. Q. Sun, and F. M. Jiang, *Heat Mass Transfer*, **50**, 1405 (2014).
34. CD-adapco, Battery Design Studio Professional © User Guide, in, 9.04.009 ed. (2014).